Nano Energy 71 (2020) 104536

Contents lists available at ScienceDirect

Nano Energy

journal homepage: http://www.elsevier.com/locate/nanoen

Full paper

Lead-free relaxor thin films with huge energy density and low loss for high temperature applications

A. Kursumovic [a,*], W.-W. Li [a], S. Cho [a,b], P.J. Curran [c], D.H.L. Tjhe [a], J.L. MacManus-Driscoll [a]

[a] Department of Materials Science and Metallurgy, University of Cambridge, 27 Charles Babbage Road, Cambridge, CB3 0FS, United Kingdom
[b] School of Materials Science and Engineering, Ulsan National Institute of Science and Technology (UNIST), Ulsan, 44919, Republic of Korea
[c] Deregallera Ltd, Unit 2 De Clare Court, Pontygwindy Industrial Estate, Caerphilly, CF83 3HU, United Kingdom

ARTICLE INFO

Keywords:
Energy storage
Relaxor ferroelectrics
Lead-free
Epitaxial perovskite
Layer by layer growth

ABSTRACT

We report record energy storage density (>80 J cm^{-3}) in Pb-free relaxor ferroelectrics based on Mn-doped $BiFeO_3$–$BaTiO_3$ thin films. Rapid interval deposition was used to impose layer-by-layer growth improving crystallinity and lowering unwanted defects concentration. The growth and Mn doping produced an order of magnitude lower leakage, with strongly reduced dielectric loss (from room temperature to >300 °C, and 100 Hz to 1 MHz), e.g. by a factor of 5 at 225 °C and 25 kHz. At room temperature (RT), the dielectric breakdown strength increased by a factor of 1.5 to >3000 kV cm^{-1} while the dielectric constant remained flat, at ~1000 from RT to 350 °C. The films perform better than competing materials (e.g. PZT and $SrTiO_3$-based) while being Pb-free and while operating up to 350 °C, which $SrTiO_3$-based systems do not. Our work gives considerable promise for high energy and power density capacitors for harsh environments.

1. Introduction

In the era of carbon reduction, many green technologies that do not generate energy on demand, require adequate energy storage. Many applications [1,2] like avionics and aerospace, automotive (under the hood power electronics in hybrid and electric vehicles), downhole drilling, mining, electromagnetic launchers and many others increasingly require the stored energy to be delivered at high power which batteries and super-capacitors alone cannot achieve. Dielectric capacitors can fill the gap necessary for these tasks, with linear high-κ dielectrics commonly used. Due to the nature of their storage, i.e. charge displacement, they are very fast to charge and discharge. Some of these applications, e.g. sophisticated drilling head machinery (for oil wells) and electric vehicles require power to be delivered at higher temperature (above ~200 °C) with a delivery rate independent on temperature and hence a flat and constant dielectric response from room temperature (RT) to higher temperatures is necessary. A high energy and power density of power electric capacitors at high temperature is very important, providing a buffer against catastrophic failure. Hence, energy storage at high temperature with long-term reliability is needed to ensure that capacitors do not need to be oversized [1].

A crucial group of properties: temperature coefficient of capacitance (TCC), dielectric loss and breakdown strength, while retaining high energy storage at high temperatures, are investigated here. Current commercial dielectrics that can work satisfactorily up to 250 °C such as Class I dielectric capacitors still have low relative dielectric constants [2] ε_r ($\equiv \kappa \sim$ 20 to 85) and consequently low volume storage capability. On the other hand, $BaTiO_3$ based Class II dielectrics have tenfold higher ε_r but are restricted to about 150 °C together with high TCC [1,2].

Among emerging materials, standard ferroelectrics, relaxor ferroelectrics and antiferroelectrics have spontaneous electric polarisation with much higher dielectric constants than standard dielectric capacitors and can work as DC and AC devices [3,4]. The main drawback of ferroelectrics is their large remnant polarisation which does not allow sufficient discharge necessary for high efficiency. Furthermore, they show low dielectric strength [5]. However, antiferroelectrics and relaxor ferroelectrics offer much larger useful energy storage [6].

Recently, a lot of effort has been paid to relaxor-ferroelectrics, which have the advantage of ferroelectrics, namely high polarizability, but at the same time rather slim hysteresis. Relaxors can be made by altering the compositions of well-researched perovskite ferroelectrics. However, the work-horse of the ferroelectrics $Pb(Zr_xTi_{1-x})O_3$ (PZT) contains lead, and so alternative lead free materials are of strong interest. Although, there are many different Pb-free material combinations that form

* Corresponding author.
E-mail address: ak237@cam.ac.uk (A. Kursumovic).

https://doi.org/10.1016/j.nanoen.2020.104536
Received 26 November 2019; Received in revised form 11 January 2020; Accepted 23 January 2020
Available online 27 January 2020

relaxors [7,8], $BiFeO_3$ (BFO) alloyed with $BaTiO_3$ (BTO) shows much promise owing to its simplicity, and its strong energy storage performance [9,10]. Alloying is needed for BFO [11,12] since while it has a large polarisation of ~100 μC cm^{-2}, and high T_c of 830 °C but has strong hysteresis and can be subject to high leakage.

Our earlier work showed excellent charge storage results in the BFO25-BTO75 composition [10]. In bulk ceramic form, upon mixing BTO with BFO, a relaxor is readily made for Bi rich compositions [13,14], and in film form the relaxor is formed over a wide BFO-BTO mixing range. We note that $SrTiO_3$ also forms a promising relaxor with BFO [10,11,15].

In this work, we strongly increase the performance of BFO25-BTO75 films. This was done by improving the crystalline perfection of the film using interval growth, as well as through introducing controlled traps for defects via Mn doping. Mn doping is known to reduce leakage considerably in titanate based ferroelectrics. For $BaTiO_3$, the formation of oxygen vacancies is facilitated by the conversion of Ti^{4+} to Ti^{3+}, and in BFO by the conversion of Fe^{3+} ions to Fe^{2+} ions [16,17]. Hence, adding Mn^{2+} to perovskites like $BiFeO_3$, $BaTiO_3$, (Ba,Sr)TiO_3 etc. leads to a manganese ion – oxygen vacancy complex which makes the oxygen vacancies less mobile and hence inactive [16,17]. In addition to the inactivating vacancies, Mn^{2+} doping of the Fe^{3+} or Ti^{4+} sites leads to hole donors which can neutralise the electrons formed as a result of positively charged oxygen vacancies as a by-product of the inherently non-equilibrium thin film growth conditions [18].

2. Material and methods

Pulsed laser deposition (PLD), with up to 50 Hz repetition rate, KrF laser ($\lambda = 248$ nm) was used to deposit the films. Conductive Nb doped $SrTiO_3$ (STO) (100) substrates were used, acting as electrodes as well as texturing templates. The substrates were hot-etched at 1000 °C and ultrasonically rinsed at room temperature in deionised-water (acid free) to achieve atomically flat surfaces and TiO_2 terminations. Using this method, safety issues of the acid-based etching process were avoided [19].

PLD targets were made in-house for the following compositions: BFO25-BTO75 with 0.5%, 2.5% and 5% Mn doping; all the doping levels are referred in molar percents. A range of doping levels was studied since the optimum Mn^{2+} doping concentration depends on the initial defect density in the film which is undetermined. Hence, to reduce leakage, breakdown field strength and loss, it is important to study different levels of Mn doping in the films. The targets were made by classical solid state reaction using stoichiometric amounts of Bi_2O_3, Fe_2O_3, $BaTiO_3$ and Mn_3O_4 with better than 3 N purity. $BaTiO_3$ was used in a nanosized form (50 nm powder); this was done to assist sintering at lower temperatures and to avoid melting of Bi_2O_3. However, 10% extra Bi added was added in order to counter its evaporation during the whole target-film processing route [10,20]. Final sintering (after calcination) was carried out at 800 °C for 2 h.

The target to substrate distance used was 55 mm; and the oxygen pressure used was 0.2 mbar. A heater temperature of 715 °C was used for the standard deposition (SD), namely slow (~0.1 nm s^{-1}) growth mode at 1 Hz repetition rate. On the other hand, 800 °C–840 °C was used for the interval mono-layer by mono-layer deposition (LLD) method.

Our hypothesis for using LLD growth is that the films should be more stoichiometric, leading to greater crystalline perfection and lower leakage. Bi-containing oxide films are very sensitive to growth conditions [21]. Hence the crystalline perfection and stoichiometry is easily compromised. Usual/standard (SD) PLD growth with a fraction of a monolayer deposited by one pulse leaves Bi atoms and/or bismuth oxide exposed to vacuum at temperatures of around 700 °C. It is well known that Bi becomes volatile and the only remedy is an excess of Bi that would eventually evaporate in ~0.1–1s time intervals during standard PLD growth. It is obvious that this stoichiometry is not easy to control. There is no theory (known to the authors) about the LLD film growth apart from estimations of the relaxation time/interval [22] necessary to facilitate "perfect" layers allowing enough time for a single layer to reconstruct towards its thermodynamically stable structure, as presented here. The higher deposition rates leave less Bi-diffusion time on the surface, while very high rates of 50 Hz enable deposition of a full monolayer (unit cell high) in 10–20 ms depending on the energy used. Large parts of Bi become entrapped in the one cell rather than on the surface. A similar situation can be modelled with a system of rate equations based on models of cosmic ice events [23], but with the addition of diffusion, as CO or CO2 in a water ice [24] resulting in a factor of five increase in the effective desorption temperature. It is obvious that such an approach in our Bi-containing films (Bi entrapment caused by high frequency/rate) in PLD bursts leads to Bi entrapment, slower desorption and hence easier to achieve better stoichiometry in the films.

For our LLD growth method, a 50 Hz burst and 1 s interval/pause was used as shown schematically in the Supplementary file (Fig. S1). In the LLD method, the ablated material in one burst deposits approximately one monolayer. Each monolayer needs to be deposited in a time shorter than the characteristic relaxation time. Hence, after this deposition, an adequate relaxation time is needed. For $SrTiO_3$ growth at 800 °C, the diffusion time is ~0.5 s and relaxation times of ~1 s are needed [25,26]. Here, for the lower melting point, Bi-containing system 1 s was expected to be sufficient for the relaxation time, particularly as transient liquid formation is possible in this system [10,27]. This method enables higher film perfection at higher growth rates because of the possibility to impose the layer by layer growth mode where otherwise island growth would occur [22]. However, for LLD the average deposition rate is set by the number of pulses necessary for 1 monolayer (dependent on the energy density and the spot size on the target), as well as the pause/interval duration.

For electrical measurements, Pt electrodes were deposited by DC-magnetron sputtering onto the film surface with shadow masks. The electrodes were from 75 to 300 μm in diameter forming a parallel plate capacitor, with the bottom electrode formed by electrically conductive Nb-doped STO substrates.

A Phillips PANalytical X-ray with CuKa radiation was used to do ω-2θ XRD scans to assess the phase purity and crystallinity of the films. A PANalytical Empyrean high resolution X-ray for the parallel plate diffractometer was used to measure reciprocal space maps (RSMs) about the (103) of STO substrates. The thickness of the films were measured by profilometry.

XPS was measured by a monochromatic Al $K\alpha_1$ X-ray source ($h\nu =$ 1486.6 eV) using a SPECS PHOIBOS 150 electron energy analyser with a total energy resolution of 500 meV. Atomic force microscopy (AFM) was done on a Bruker MultiMode 8 Nanoscope III in tapping mode.

The leakage current was measured using a two-probe station and a Keithley 2440 source-meter. A Radiant 100 Precision ferroelectric tester was used to measure polarisation vs. electric field (i.e. *P-E* hysteresis loops). An HP 4294A Impedance Analyser was used to measure dielectric constant as well as dielectric loss and other AC properties from 40 Hz up to 100 MHz, as a function of temperature while samples were mounted on a hot plate. A 50 mV signal was used for most of the impedance measurements. The top electrode (Pt) defines the parallel plate capacitor geometry from which the relative dielectric constant ε_r of the measured film is calculated from its capacitance: $C = \varepsilon_r \times \varepsilon_0 \times A/d$, where $\varepsilon o = 8.854 \times 10^{-12}$ F m^{-1} is the vacuum permittivity, A is the overlapping surface area of the plate and the bottom electrode (conductive substrate here) and d is the distance between the plates (i.e. film thickness).

The breakdown strength was estimated by either the penultimate field step before breakdown during DC leakage current measurements or from the 1 kHz *P-E* loop measurements, averaging by more than 10 points (electrodes).

3. Results and analysis

3.1. XRD, AFM and XPS data

First, we compare the alignment and crystalline perfection of the films. Fig. 1a shows a narrow region of the θ-2θ scans of the films using pulsed laser deposition (PLD) in a standard (SD) mode compared to the layer by layer (LLD) deposited films (Fig. 1a). Both show excellent (00*l*) alignment with no evidence for other orientations (full XRD scans are shown in Supplementary Fig. S2). A magnified view of the Bragg Bretano plot showing the (002) film peak is given in Fig. 1a. It is observed that the LLD film peak is shifted to lower angle than the SD peak indicating a higher *c* axis (the XRD results are summarized in Table 1). The PLD SD and LLD modes are detailed in the Materials and Methods section.

As shown in Fig. 1b, the *out-of-plane* rocking curve (ω scan) of the LLD film is much sharper than the SD film (0.2° cf. 0.5°), despite the ~5 × faster growth rate. This is related to the growth mechanism of the layer-by-layer grown films where a single cell thick 2D mode is imposed [22]. Furthermore, the process should enable better stoichiometric transfer of Bi which is often lost to some degree in Bi-containing films. Shortened surface residence time (due to full unit cell deposition in a short time) makes volatile atoms less exposed to surface diffusion and eventual desorption.

It is clear that better crystalline perfection is achieved for the LLD film compared to the SD film. This is also observed by comparing reciprocal space maps (RSMs, Fig. 2c and d) for the 2 films, which have FWHM values of the q_x scans of 0.037° vs. 0.047°. The RSM maps also show that in both cases the films are relaxed as the RSM peaks for the film are far to the left of the substrate peak along q_x.

We note that regardless of the Mn-dopant concentration, all interval (LLD) growth films exhibited more uniform *in-plane* and *out-of-plane* lattice parameters, and ultimately better crystalline perfection. Also, from AFM images (Fig. 1e and f), LLD growth gives much more uniform surface features/grains as well as much lower roughness than SD growth, i.e. 2 nm *rms* vs. 5 nm *rms*, respectively, for ~100 nm thick films.

It is observed that the LLD film peak is shifted to lower angle than the SD peak for the films (2.5% Mn doped), indicating a higher *c* axis (the XRD results are summarized in Table 1). On the other hand, for the case of 0.5% Mn-doping both SD and LLD films have their (002) peaks at almost the same position as LLD films for 2.5% Mn (lattice parameter data in Table S1 in the Supplement). From this we can conclude that both Mn doping and growth method cause a peak shift. For the 2.5% Mn doping, the difference in peak positions corresponds to a lattice parameter difference of 0.0093 ± 0.0012 Å. This *c*-axis increase by Mn doping is in agreement with the literature for Mn doping of BTO based solid solutions (for Mn < 4% in ceramics [28] and for Mn < 6% in thin films [29]), where the *c*-axis increases with Mn doping.

The effectiveness of Mn doping was measured using X-ray photoelectron spectroscopy (XPS), as shown in Fig. 2. The Fe $2p_{3/2}$ peaks were fitted by XPS built in program; the Fe^{2+} and Fe^{3+} peaks are located at 709.85 eV and 710.95 eV respectively. The results show that low doping

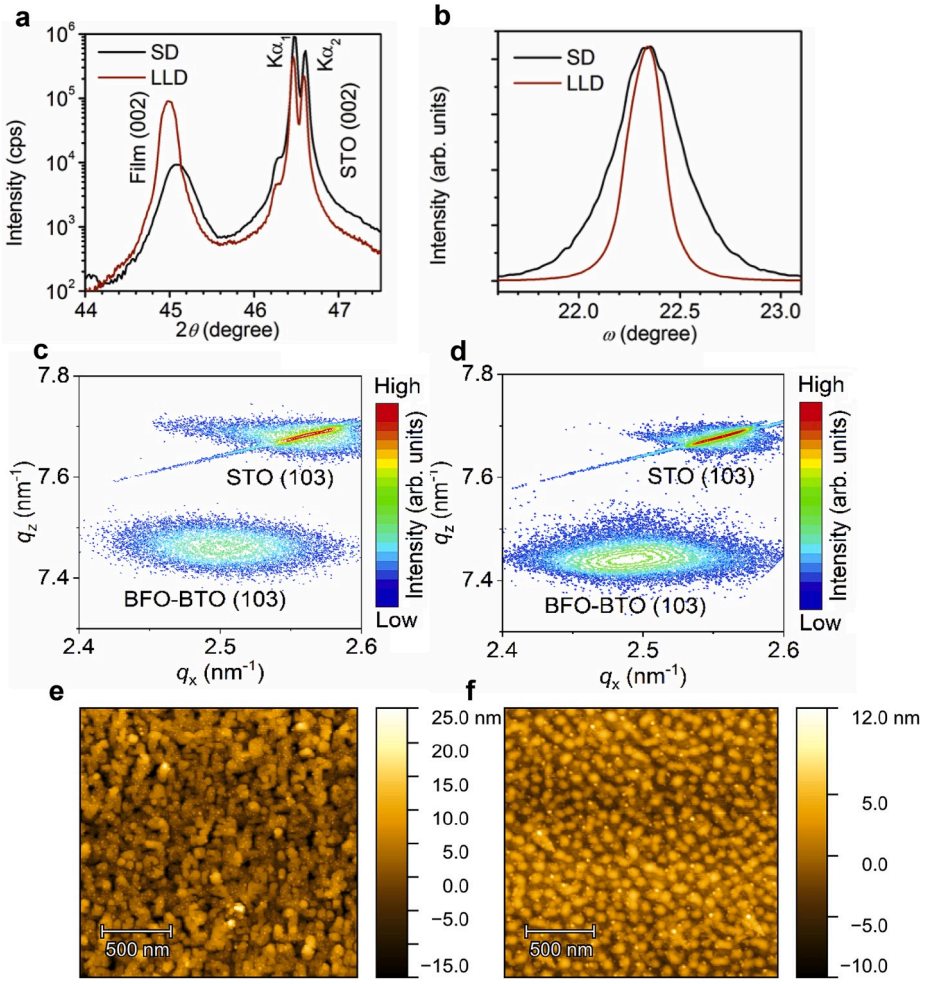

Fig. 1. Structural data of 2.5% Mn-doped films. a) 2θ XRD scans of SD and LLD films around (002) peak. b) ω (002) XRD scans of the SD and LLD films from a). c) RSM map of the SD film near the STO (103) reflection. d) RSM map of the LLD film around the STO (103) reflection. Tapping mode AFM images over a large scan area films: e) SD film with σ_{rms} ~5 nm and f) LLD film with lower σ_{rms} ~2 nm and more uniform grain sizes.

Table 1
Parameters for (2.5% Mn-doped) films made by standard (SD) and layer by layer (LLD) deposition by pulsed laser deposition in this work for 350 nm thick films.

Growth type	Growth time (s)	2θ-FWHM (°)	Thickness (nm)	ω-FWHM (°)	q_x-FWHM (nm^{-1})	q_z-FWHM (nm^{-1})
SD	3600	0.29	350	0.5	0.047	0.02
LLD	900	0.13	350	0.2	0.037	0.04

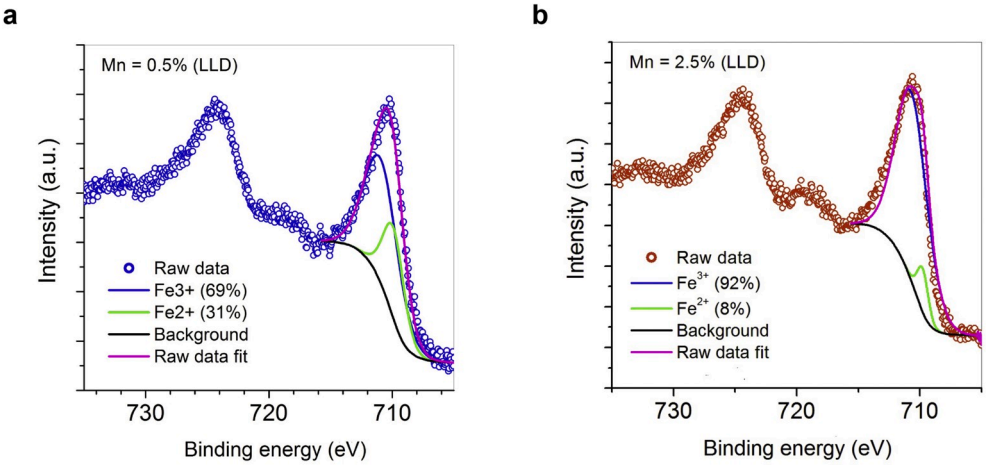

Fig. 2. Effect of Mn content on Fe ionization in LLD 25BFO-75BTO films as determined from XPS spectra. a) 0.5% Mn doped LLD film. The Fe^{2+} content was ~31%. This is similar to the un-doped film - not shown); b) 2.5% Mn doped LLD film. The Fe^{2+} content is reduced significantly (to ~8%) compared to the 0.5% Mn doped film.

(0.5% Mn) does not reduce the Fe^{2+} amount (it is around 30%). However, 2.5% Mn doping significantly reduces Fe^{2+} to about 8%, by blocking formation of oxygen vacancies. This would be expected to reduce the leakage in the films. This is indeed the case, as we show later. Titanium was 100% in the Ti^{4+} state regardless of doping (not shown).

3.2. Leakage current

It is well known that leakage is a problem for thin film epitaxial ferroelectrics, and especially in BFO based materials [30,31]. Leakage also impacts on dielectric breakdown strength and loss, and hence it is important to minimize this parameter first. We determined that the optimal doping range for the films is 2.5% Mn. The leakage for 2.5% Mn doped films is determined, comparing growth by SD and LLD, from *J-V* plots in Fig. 3a. The leakage current is observed to be an order of magnitude lower for the LLD film which is as expected based on its higher perfection and alignment. This agrees with earlier work that shows that leakage current in BFO can be drastically reduced by controlling kinetic growth parameters [32]. Confirmation that for LLD growth 2.5% Mn doping is optimal in Fig. 3b we compare *J-V* plots for 0.5% Mn and 2.5% Mn doping (note we do not show 5% Mn as this film had considerably higher leakage consistent with earlier reports [33] in $(Ba,Sr)TiO_3$). Again, over most of the field range, over an order of magnitude reduced leakage current is achieved.

3.3. Dielectric constant and dielectric loss

Dielectric losses are intimately connected with dipole relaxation occurring as a response to an applied AC electric field [34]. The dielectric losses (tan δ) of the 0.5% Mn doped and 2.5% Mn doped films were extracted directly from impedance data. Representative impedance data with fittings of the data is shown in the Supplementary Fig. S3. In Fig. 4a, the dielectric loss of our doped films is compared at 25 kHz frequency with our optimised undoped films reported previously [10]. It can be seen that below 225 °C, tan δ for 0 and 0.5% Mn doping is $> 10^{-2}$ while for 2.5% Mn doping it is reduced by up to a factor of 5.

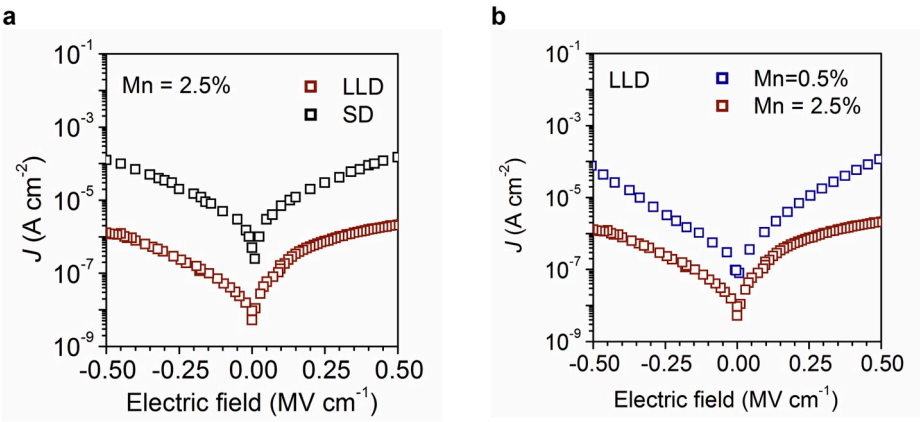

Fig. 3. a) Leakage current of optimally doped (2.5% Mn) BFO-BTO SD film versus optimally doped LLD film. b) Room-temperature leakage current for LLD films with two distinctive levels of Mn doping.

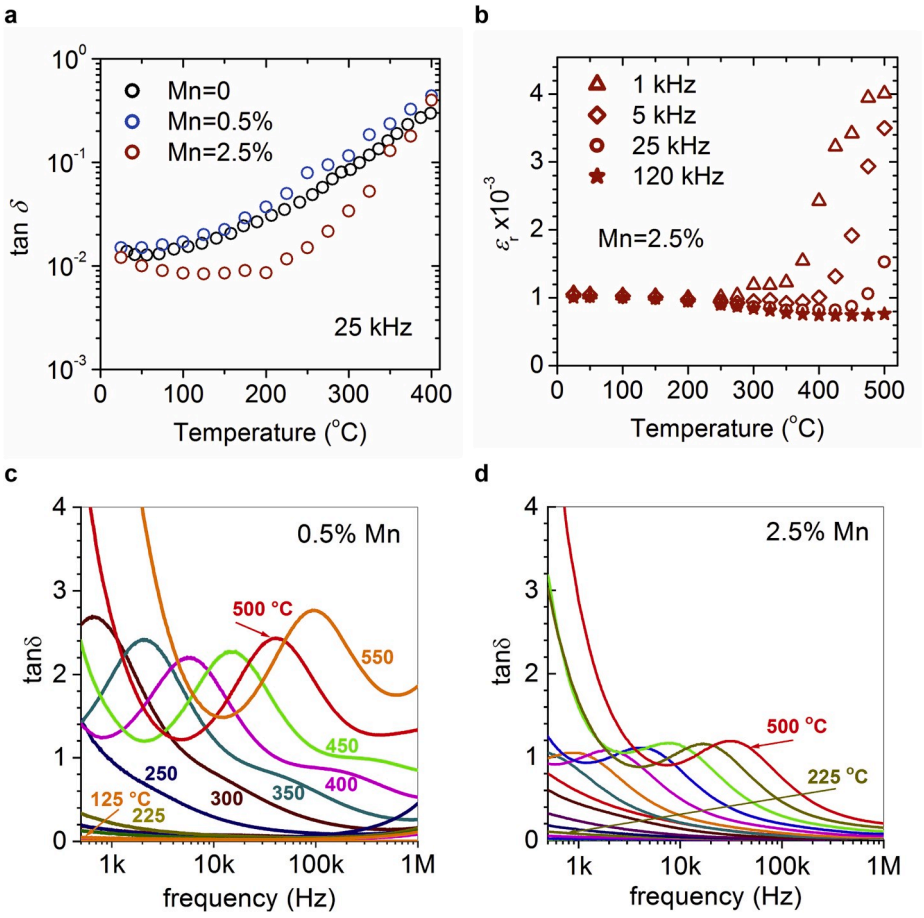

Fig. 4. a) Dielectric loss of 2.5% Mn doped LLD film. The loss at 25 kHz is compared with our earlier work on undoped films [10]. b) Dielectric constant ε_r of the 2.5% Mn doped BFO25-BTO75 film grown by LLD. c) Dielectric loss, tan δ, of the 0.5% Mn doped sample; above 250 °C the temperature interval is 50 °C. d) Dielectric loss of the 2.5% Mn doped sample; the temperature interval is 25 °C.

In Fig. 4b, we focus on the relative dielectric constant ε_r as a function of frequency and temperature of the 2.5% Mn doped sample which showed the superior loss performance over 0.5% Mn (Fig. 4a). An almost temperature independent trend in ε_r (calculated from the measured capacitance C_p in assumed configuration parallel to a leakage resistance, hence C_p) from room temperature to above 350 °C is observed, as for undoped BFO25-BTO75 as we reported previously [10] but with twice the value of the relative dielectric constant, i.e. at 25 kHz, ε_r~1000 for 2.5% Mn doped much the same as in un-doped samples [10]. This flat behaviour of ε_r with temperature shows the strong potential of the material for high temperature capacitors. Furthermore, the temperature of the peak in ε_r compared to undoped sample has shifted to higher temperatures, and to an increasing extent as the frequency increases, indicating relaxor behaviour [10].

Looking in more detail at the frequency dependence of tan δ, comparing the 0.5% Mn doped (Fig. 4c) and 2.5% Mn doped (Fig. 4d) films we observe that at as high as 225 °C flat behaviour is achieved for the 2.5% Mn sample, all the way from 1 MHz to 1 KHz, whereas for the 0.5% Mn doped sample the loss is flat only below ~125 °C. This frequency dependence of loss has not been shown before in this system, but it is extremely important for high temperature operation of the material. For many applications, loss needs to be minimised at low frequencies as well as high frequencies, e.g. for power delivery in the automotive industry. The reason for the shift of the tan δ peak to lower frequency in the 2.5% Mn doped sample (giving lower high temperature tan δ over a wide frequency range) is explored later by analysing the AC conduction.

3.4. *P-E loops, breakdown strength and storage properties*

The polarisation values and the dielectric breakdown are key factors that define the storage capacity of a parallel plate capacitor since energy W is an integral above the discharging curve. Fig. 5 shows polarisation versus electric field (*P-E*) loops for a 2.5% Mn doped film for different maximum applied voltages. Fig. 5a shows both + and – applied electric fields, and Fig. 5b shows a region of the positive quadrant of the loop showing the recovered energy. The maximum polarisation shows some deviations (from the nested loops) at high fields (at ±120 V and ±100 in Fig. 5a) (lower maximum polarisation value). This is likely to be due to distortion caused by the contact deterioration at very high fields (effectively reducing the surface area and/hence the apparent polarisation).

From Fig. 5b, we determine a very high energy storage density, W, of up to 80 J cm^{-3} at 3.1 MV cm^{-1} The value was obtained by the standard integration for the room temperature data (green in Fig. 5b). This is 50% higher energy than we observed previously for standard deposited undoped BFO-BTO films [10]. The result was achieved because of the higher breakdown field strength (estimated from Fig. 5a here) ~ 3 MV cm^{-1} compared to ~ 2 MV cm^{-1} without Mn doping [10]. The efficiency (η) was obtained dividing the energy storage density with the integral that included the hysteresis loss (purple in Fig. 5b), giving η = 78% at 3.1 MV cm^{-1}. At the lower field of 2.75 MV cm^{-1}, W is lower (>72 J cm^{3}), due to lower field applied, while η is higher (88%).

Our room temperature energy storage results are compared to literature data in Fig. 6. The plot shows the general trend of increased energy storage with increasing electric field. Our energy storage value is

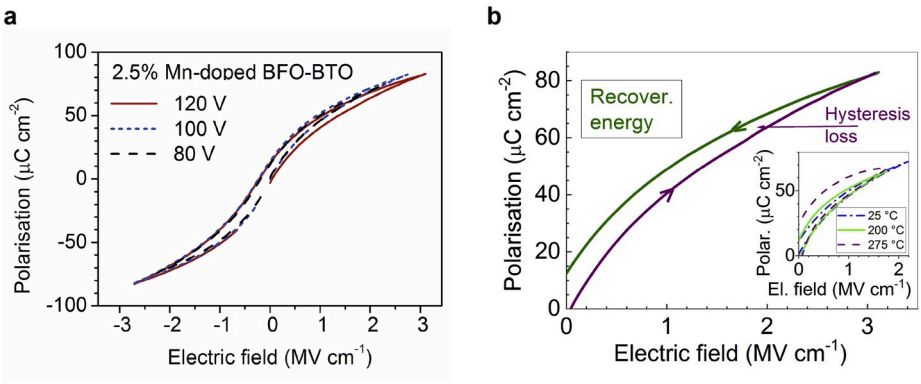

Fig. 5. a) Room temperature ferroelectric polarisation versus applied electric field (*P–E*) plot for 2.5% Mn doped BFO25-BTO75 film measured at 1 KHz. The slim shape of the loop indicates the relaxor dielectric behaviour. b) Energy stored and lost shown on the *P-E* plot for the 2.5% Mn doped film of a). The energy stored calculated for an applied electric field of 3.10 MV cm^{-1} (near dielectric breakdown strength) is 80 J cm^{-3}. The inset to b) shows the polarisation at higher temperatures (with max. 60 V applied). A visibly distorted *P-E* loops starts to develop above 200 °C.

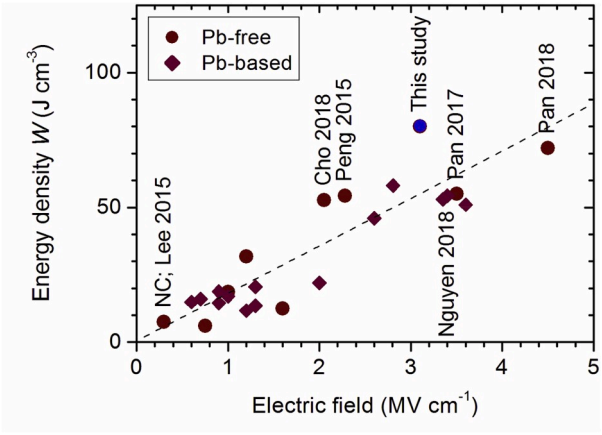

Fig. 6. Energy densities, *W*, of the films compiled from the relevant literature. The leading literature results, as standard *P-E* loops, are shown. Our previous results [10] are also included. Our 80 J cm^{-3} values exceed the maximum value of 70 J cm^{-3} reported previously [11] although our maximum electric field is lower.

the highest reported (>80 J cm^{-3}) for a high temperature ferroelectric film. On the other hand the results of Pan's et al. [11] on $BiFeO_3$–$SrTiO_3$ (BFO-STO) films are at a higher breakdown field of over 4 MV cm^{-1} which is expected because of use of the BFO-STO alloy [11] rather than our BFO-BTO alloy, since STO has a lower dielectric constant than BTO, i.e. <200 cf. ~1000 [35]. For a wide range of high-κ dielectrics a lower dielectric constant leads to a higher breakdown strength [36,37]. However, our energy density is above the general trend line. This is likely a result of our *combined* defect engineering approach (highly perfect films by LLD growth, plus introduction of traps from Mn^{2+} dopants) when compared to Ref. [10]. If the breakdown strength were increased further, we would expect to stay above the standard line, thus giving the prospect of an even higher energy storage above 4 MV cm^{-1}. This may be achieved by alloying with STO, to form a STO-BTO-BFO alloy.

The *P-E* loops at higher temperatures begin to be increasingly affected by the increased leakage current, misrepresenting the effect of leakage current as part of polarisation [38,39]. This affects the estimation of the energy density and the efficiency, showing incorrectly lower values for both. This can be seen for the 275 °C loop (in inset to Fig. 5b) with apparently doubled hysteresis loss versus the 25 °C one. At high temperatures (at least up to 275 °C, inset to Fig. 5b) the (increased) leakage would need to be measured simultaneously with the polarisation (*P*) to find its contribution to the measured *P* value and calculate the real energy storage and its efficiency, which are still projected to be of a similar very high values of W > 70 J cm^{-3} and η > 80%, respectively. In fact, high temperature energy density and efficiency are hardly ever investigated, so it is difficult to compare our result with other materials.

3.5. Discussion on AC and DC conducting mechanisms

We now turn to understanding more about how our combined defect engineering approach has led to the improved energy storage that we have achieved. We do this by analysing both DC and AC conduction data. *J-V* curves under DC measurements allow us to determine the conducting mechanisms limiting the current and hence the origin of the leakage and the DC component to the loss. However, the DC measurements do not show the full spectrum of conductivity mechanisms and so we turn to AC measurements to probe these. Looking first at the DC measurements, Supplementary Fig. S4 shows a *J-V* plot at room temperature together with analysis of the different field regimes.

We consider the space charge limited conduction (SCLC) regime where carriers fill the traps (between the valence and the conduction bands). This occurs (Supplementary Fig. S4) at around 50–1000 kV cm^{-1}. Fig. 7 shows an Arrhenius plots of DC conductivity versus inverse temperature at 300 KV cm^{-1}, determined from *J-V* plots measured at different temperatures. Activation energies, ΔE_σ, of 0.53–0.57 eV were obtained for the different doping levels (0, 0.5 and 2.5% Mn). These values are found to be consistent with the motion of oxygen vacancies in similar systems [40] suggesting the leakage mechanism in this regime, is related to the presence of oxygen vacancies. However, singly ionized vacancies would show [40] lower activation energies than doubly ionized ones, as 0.3–0.4 eV versus 0.6–1.2 eV, respectively. Hence, our DC leakage would be mostly due to singly charged vacancies (Fig. 7a). The different levels of DC conductivity (i.e. lower for increased doping) indicates that Mn is changing the pre-exponential factor in the conductivity. Hence, increasing Mn doping does not change the mechanism of conduction, but it leads to an increased trap density.

To learn about dielectric losses we turn to the AC measurements, i.e. AC impedance analysis (example impedance plots are shown in Supplementary Fig. S3) which gives information on the nature of the relaxation and resulting losses. In each spectrum we observe a high frequency semicircle, which is related to the bulk material, and a low frequency one which is associated with the interface between the sample and the electrode. The low frequency semicircle is not of interest to us here. The high frequency semicircles are depressed, i.e. with their centres below "zero", indicative of a distribution of relaxation times. This is discussed in more detail in Supplementary Note 3. The real impedance, Re(Z), imaginary impedance, Im(Z). apex values and corresponding angular frequencies were extracted from the plots. The peak frequencies were similar in both cases, but the resistance values were almost an order of magnitude higher for the 2.5% Mn sample, in agreement with the lower leakage measured from the DC measurements (Fig. 3b).

From impedance measurements made over a range of temperatures from 250 °C to 550 °C, an Arrhenius plot of the loss relaxation time

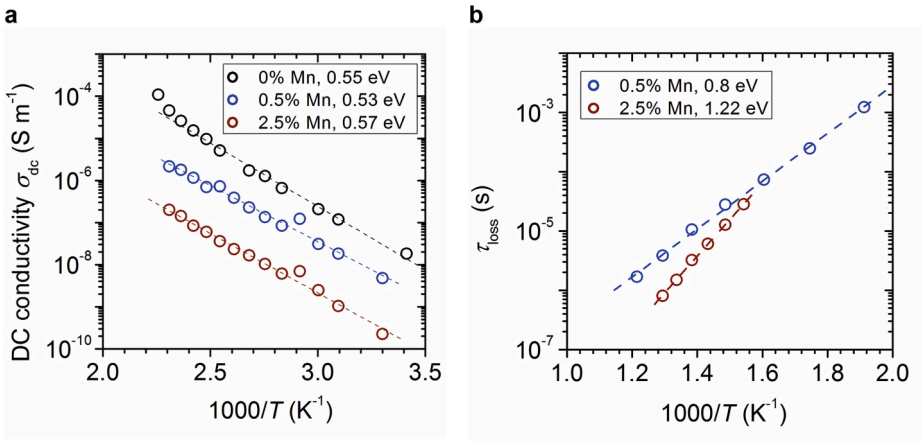

Fig. 7. a) Arrhenius plot (leakage conductivity) of the films with different Mn doping level. b) Loss peak activation energies for 0.5% and 2.5% Mn doped samples.

(determined from the apex of the high frequency semicircles data) τ_{loss} = R·CPE (of the peak value in Supplementary Fig. S3) versus inverse temperature is shown in Fig. 7b. For the 0.5% Mn doped sample, the activation energy is close to the DC measured activation barrier of Fig. 7a (0.53 eV *cf*. 0.8 V). The data is compared in Table 2. Although there are different ionization levels both mechanisms seem to originate from the presence of oxygen vacancies. The similar values indicate the same loss mechanism.

For the 2.5% Mn doped sample, the activation energy at temperatures below 600 °C is much larger than for the activation energy measured at DC (1.22 eV vs. 0.57 eV), as shown in Table 2. This indicates a higher level of ionization in the higher Mn doped films. We note only low temperature measurements could be made because higher temperatures would require much lower frequencies for the measurements.

The very different activation energies for the 0.5% and 2.5% Mn doped samples indicate that at 2.5% doping there is a sufficient concentration of defect complexes to change the loss mechanism, and indeed to strongly reduce the AC losses. For the 2.5% Mn doped sample the activation energy is consistent with dissociation of the defect complexes introduced by doping, as was shown previously [41] for $BaTiO_3$. It is likely that Mn has a pinning effect on the polar nanoregion dipole oscillations, thus reducing the loss [42].

In summary, the low doping levels do not influence the loss mechanism (since the DC and AC behaviour is the same) but high defect concentrations influence the dipole oscillation mechanism significantly. It has been shown previously that for dielectric relaxation in relaxors, a stretched-exponential relaxation appears as a consequence of non-Debye behaviour [43]. We observe such a stretched-exponential via our depressed impedance semi-circles, for both 0.5% and 2.5% Mn doped films. This type of relaxation is intimately related also to the peculiar lattice dynamics of glasses. Hence, our data for the 2.5% Mn doped sample is consistent with a highly disordered glass-like systems.

4. The implications of the low dielectric loss

As mentioned in the introduction, the two key requirements for capacitors are high energy density and high power density. Here, we reached a record energy density value of 80 J cm^{-3}, with an efficiency of almost 90%, at electric breakdown fields E_{bd} > 3 MV cm^{-1}. This is very relevant for DC applications. However, for AC applications and high current impulse events (ultra-fast charge-discharge capability), the power density becomes equally or even more important. It is assumed that high power density (~10^8 W cm^{-2}) in ceramic capacitors is retained in thin films as well. Analytically, the maximum power density in a simple (linear) capacitor at an effective frequency f is [44]: $P_{max} = \pi f \varepsilon_r \varepsilon_0 E_{bd}^2/(2\tan\delta)$. This equation emphasizes the importance of a low value of tan δ. Here we have reduced tan δ by more than 5 × times compared to the other best high energy density films [11,15]. This is therefore significant for short time delivery, high power density applications.

On the other hand, it should be emphasized that our BFO-BTO films exhibit a relative permittivity ε_r~1000 and a temperature variation of capacitance C (ΔC/C) of 9% up to 330 °C (using the EIA- RS-198 system [1,2,45,46]). For comparison, current market leading Class I materials have ΔC/C) = 15% from −55 °C to 200 °C and typically have ε_r ~30 [46], hence our material is in principle has ~33 (1000/30) times more energy dense and power efficiency (having lower volume for the same effect). Current Class II X8R dielectrics ($BaTiO_3$-based) have ε_r~3000 but are restricted to operation below 150 °C.

Table 2
Activation energies determine from the DC and AC measurements.

Doping	E_A from DC conduction (eV)	E_A from AC conduction (eV)
0% Mn	0.57	–
0.5% Mn	0.53	0.80
2.5% Mn	0.57	1.22

5. Conclusions

We have applied a combined defect engineering approach to high energy storage relaxor ferroelectric $(BiFeO_3)_{0.25}(BaTiO_3)_{0.75}$ (BFO25-BTO75) thin films to achieve a record energy storage capacity of >80 J cm^{-3}. The combined approach involves a fast interval growth process to achieve much more crystalline material, along with Mn doping (2.5% Mn being optimum) to introduce trap states. The approach leads to strongly reduced leakage and reduced loss. The leakage reduction enables a 50% higher breakdown field to be achieved, > 3 MV cm^{-1}, compared to undoped material, thus enabling a wider region of *P-E* space to be accessed, giving higher energy storage. The loss reduction enables the material to be operated to higher frequencies and to higher temperatures. Notably, for the first time a low and flat loss of <0.01 has achieved up to 225 °C, and down to as low as 100 Hz. Also, the dielectric constant remains flat over a wide frequency range, up to 350 °C. Our data lies above the standard linear plot relating energy storage versus maximum electric field applied, indicating the benefits of the defect engineering approach. Using our method, there is much further potential for the BFO-BTO system to have higher energy storage if STO is also mixed in to the film. Also, further optimisation will come from optimising the interface of film and electrode to maximise space charge limiting conduction.

Declaration of competing interest

The authors declare that they have no known competing financial interests or personal relationships that could have appeared to influence the work reported in this paper.

Acknowledgements

We acknowledge funding support from EPSRC grants EP/N004272/1, EP/M000524/1, and EP/L011700/1, the Leverhulme Trust grant RPG-2015-017, the Winton Foundation and Deregallera Ltd., United Kingdom.

Appendix A. Supplementary data

Supplementary data to this article can be found online at https://doi.org/10.1016/j.nanoen.2020.104536.

References

[1] X. Xu, A.S. Gurav, P.M. Lessner, C.A. Randall, Robust BME Class-I MLCCs for harsh-environment applications, IEEE Trans. Ind. Electron. 58 (2011) 2636.
[2] A.V. Polotai, S.G. Maher, J.M. Wilson and R.G. Maher, Selection of dielectric materials for high temperature applications, March 15-18, 2010 CARTS USA 2010 Proceedings, p. 249-262 New Orleans, LA.
[3] W. Känzig, Solid State Physics: Advances in Research and Applications, vol. 4, Academic Press Inc, New York, 1957.
[4] M. Lines, A. Glass, Principles and Applications of Ferroelectrics and Related Materials, Clarendon Press, Oxford, 1979.
[5] N. Ortega, A. Kumar, J.F. Scott, D.B. Chrisey, M. Tomazawa, S. Kumari, D.G. B. Diestra, S. Katiyar, Relaxor-ferroelectric superlattices: high energy density capacitors, J. Phys. Condens. Matter 24 (2012) 445901.
[6] P. Mohapatra, Z. Fan, J. Cui, X. Tan, Relaxor antiferroelectric ceramics with ultrahigh efficiency for energy storage applications, J. Eur. Ceram. Soc. 39 (2019) 4735.
[7] Z. Tang, J. Ge, H. Ni, B. Lu, X.-G. Tang, S.-G. Lu, M. Tang, J. Gao, High energy-storage density of lead-free $BiFeO_3$ doped Na0.5Bi0.5TiO_3-$BaTiO_3$ thin lm capacitor with good temperature stability, J. Alloys Comp. 757 (2018) 169.
[8] L. Zhang, Y. Pu, M. Chen, G. Liu, Antiferroelectric-like properties in MgO-modified 0.775$Na_{0.5}Bi_{0.5}TiO_3$-0.225$BaSnO_3$ ceramics for high power energy storage, J. Eur. Ceram. Soc. 38 (2018) 5388.
[9] K. Yao, S. Chen, M. Rahimabady, M.S. Mirshekarloo, S. Yu, F.E.H. Tay, T. Sritharan, L. Lu, Nonlinear dielectric thin films for high-power electric storage with energy density comparable with electrochemical supercapacitors, IEEE Trans. Ultrason. Ferroelectrics Freq. Contr. 58 (2011) 1968.
[10] S. Cho, C. Yun, Y.S. Kim, H. Wang, J. Jian, W. Zhang, J. Huang, X. Wang, H. Wang, J.L. MacManus-Driscoll, Strongly enhanced dielectric and energy storage properties in lead-free perovskite titanate thin films by alloying, Nano Energy 45 (2018) 398.
[11] H. Pan, Y. Zeng, Y. Shen, Y.-H. Lin, J. Ma, L. Li, C.-W. Nan, $BiFeO_3$–$SrTiO_3$ thin film as a new lead-free relaxor ferroelectric capacitor with ultrahigh energy storage performance, J. Mater. Chem. A 5 (2017) 5920.
[12] E. Khomyakova, M. Sadl, H. Ursic, J. Daniels, B. Malic, A. Bencan, D. Damjanovic, T. Rojac, Self-poling of $BiFeO_3$ thick films, ACS Appl. Mater. Interfaces 8 (2016) 19626.
[13] Y. Wang, Y. Pu, Xin Li, H. Zheng, Z. Gao, Evolution from ferroelectric to diffused ferroelectric, and relaxor ferroelectric in $BaTiO_3$-$BiFeO_3$ solid solutions, Mater. Chem. Phys. 183 (2016) 247.
[14] D. Wang, G. Wang, S. Murakami, Z. Fany, A. Feteiraz, D. Zhoux, S. Sun, Q. Zhao, I. M. Reaney, $BiFeO_3$-$BaTiO_3$ A new generation of lead-free electroceramics, J. Adv. Dielectr 8 (2018) 1830004.
[15] H. Pan, J. Ma, J. Ma, Q. Zhang, X. Liu, B. Guan, L. Gu, X. Zhang, Y.-J. Zhang, L. Li, Y. Shen, Y.-H. Lin, C.-W. Nan, Giant energy density and high efficiency achieved in bismuth ferrite-based film capacitors via domain engineering, Nat. Commun. 9 (2018) 1813.
[16] G.W. Pabst, L.W. Martin, Y.-H. Chu, R. Ramesh, Leakage mechanisms in $BiFeO_3$ thin films, Appl. Phys. Lett. 90 (2007), 072902.
[17] K. Nadaud, C. Borderon, R. Renoud, H.W. Gundel, Effect of manganese doping of $BaSrTiO_3$ on diffusion and domain wall pinning, J. Appl. Phys. 117 (2015), 084104.
[18] A.L. Sangle, O.J. Lee, A. Kursumovic, W. Zhang, A. Chen, H. Wangand, J. L. MacManus-Driscoll, Very high commutation quality factor and dielectric tunability in nanocomposite $SrTiO_3$ thin films with T_c enhanced to >300 °C, Nanoscale 10 (2018) 3460.
[19] J.G. Connell, B.J. Isaac, G.B. Ekanayake, D.R. Strachan, S.S.A. Seo, Preparation of atomically flat $SrTiO_3$ surfaces using a deionized-water leaching and thermal annealing procedure, Appl. Phys. Lett. 101 (2012) 251607.
[20] X. Xie, S. Yang, F. Zhang, S. Fan, Q. Che, C. Wang, X. Guo, L. Zhang, Effects of excess Bi on structure and electrical properties of $BiFeO_3$ thin films deposited on indium tin oxide substrate using sol–gel method, J. Mater. Sci. Mater. Electron. 26 (2015) 10095.
[21] M. Lorenz, V. Lazenka, P. Schwinkendorf, F. Bern, M. Ziese1, H. Modarresi, A. Volodin, M.J. Van Bael, K. Temst, A. Vantomme, M. Grundmann, Multiferroic $BaTiO_3$–$BiFeO_3$ composite thin films and multilayers: strain engineering and magnetoelectric coupling, J. Phys. D Appl. Phys. 47 (2014) 135303.
[22] D.H.A. Blank, G. Koster, G.A.J.H.M. Rijnders, E. van Setten, P. Slycke, H. Rogalla, Epitaxial growth of oxides with pulsed laser interval deposition, J. Cryst. Growth 211 (2000) 98.
[23] T.I. Hasegawa, E. Herbst, Three-phase chemical-models of dense interstellar clouds - gas, dust particle mantles and dust particle surfaces, Mon. Not. Roy. Astron. Soc. 263 (1993) 589.
[24] E.C. Fayolle, K.I. Oeberg, H.M. Cuppen, R. Visser, H. Linnartz, H.2O. Laboratory, CO_2 ice desorption data: entrapment dependencies and its parameterization with an extended three-phase model, Astron. Astrophys. 529 (2011) A74.
[25] G. Koster, G.J.H.M. Rijnders, D.H.A. Blank, H. Rogalla, In situ initial growth studies of $SrTiO_3$ on $SrTiO_3$ by time resolved high pressure RHEED, Mater. Res. Soc. Symp. Proc. 526 (1998) 33.
[26] G. Koster, G.J.H.M. Rijnders, D.H.A. Blank, H. Rogalla, Imposed layer-by-layer growth by pulsed laser interval deposition, Appl. Phys. Lett. 74 (1999) 3729.
[27] M. Li, A. Kursumovic, X. Qia, J.L. MacManus-Driscoll, Rapid epitaxial growth of magnetoelectric thick $BiFeO_3$ films by hybrid liquid-phase epitaxy, J. Cryst. Growth 293 (2006) 128.
[28] N.V. Dang, T.-L. Phan, T.D. Thanh, V.D. Lam, L.V. Hong, Structural phase separation and optical and magnetic properties of $BaTi_{1-x}MnxO_3$ multiferroics, J. Appl. Phys. 111 (2012) 113913.
[29] X. Chen, C. Yang, M. Fan, Z. Xu, J. Zhu, P. Yu, Characterization of manganese ions in Mn substituted $Ba_{0.67}Sr_{0.33}Mn_xTi_{1-x}O_3$ thin films, Ferroelectrics 454 (2013) 129.
[30] X. Qi, J. Dho, R. Tomov, M.G. Blamire, J.L. MacManus-Driscoll, Greatly reduced leakage current and conduction mechanism in aliovalent-ion-doped $BiFeO_3$, Appl. Phys. Lett. 86 (2005), 062903.
[31] H. Zhu, H. Ma, Y. Zhao, Role of rapid and slow cooling on leakage mechanism and ferroelectric polarization of sputtered epitaxial $BiFeO_3$ thin films, Vacuum 163 (2019) 312.
[32] V. Shelke, V.N. Harshan, S. Kotru, A. Gupta, Effect of kinetic growth parameters on leakage current and ferroelectric behavior of $BiFeO_3$ thin films, J. Appl. Phys. 106 (2009) 104114.
[33] Y. Ito, W. Sakamoto, M. Moriya, T. Yogo, Synthesis and properties of multiferroic 0.7$BiFeO_3$-0.3$BaTiO_3$ thin films by Mn doping, Ceram. Int. 39 (2013) S451.
[34] L. Zhu, Q. Wang, Novel ferroelectric polymers for high energy density and low loss dielectrics, Macromolecules 45 (2012) 2937.
[35] K. Ikuta, Y. Umeda, Y. Ishii, High-frequency characteristics of $SrTiO_3$ thin films in the mm-wave band, Jpn. J. Appl. Phys. 35 (1996) 1513.
[36] J. McPherson, J. Kim, A. Shanware, H. Mogul, J. Rodriguez, Proposed universal relationship between dielectric breakdown and dielectric constant, in: Conference: IEEE Internat. Electron Devices 2002 Meeting, San Francisco, CA, Dec 08-11, 2002, Technical Digest, 2002, p. 633.
[37] L. Yang, X. Kong, F. Li, H. Hao, Z. Cheng, H. Liu, J.-F. Li, S. Zhang, Perovskite lead-free dielectrics for energy storage applications, Prog. Mater. Sci. 102 (2019) 72.
[38] M. Brazier, S. Mansour, E. Paton, M. Mcelfresh, Effects of finite electrical resistance on the polarization measurement of ferroelectric capacitors, Integr. Ferroelectrics 18 (1997) 79.
[39] J.T. Evans, Characterizing Ferroelectric Materials, Radiant Technologies, Inc, March 7, 2011. https://www.ferrodevices.com/1/297/files/Ferroelectric_Properties_and_Instrumentation(1).pdf. (Accessed 28 December 2019).
[40] B. Kaur, L. Singh, V.A. Reddy, D.-Y. Jeong, N. Dabra, J.S. Hunda, AC impedance spectroscopy, conductivity and optical studies of Sr doped bismuth ferrite nanocomposites, Int. J. Electrochem. Sci. 11 (2016) 4120.
[41] S.J. Lee, S.M. Park, Y.H. Han, Dielectric relaxation of Al-doped $BaTiO_3$, Jpn. J. Appl. Phys. 48 (2009), 031403.
[42] L. Cai, R. Pattnaik, J. Lundeen, J. Toulouse, Piezoelectric polar nanoregions and relaxation-coupled resonances in relaxor ferroelectrics, Phys. Rev. B 98 (2018) 134113.
[43] B. Cui, R. Milkus, A. Zaccone, The relation between stretched-exponential relaxation and the vibrational density of states in glassy disordered systems, Phys. Lett. A381 (2017) 446.
[44] D.-H. Choi Randall, E. Furman, B. Ma, U.B. Balachandran, S. Zhang, M. Lanagan, in: Conference: IEEE International Workshop on Integrated Power Packaging (IWIPP) Chicago, IL, MAY 03-06, 2015.
[45] Ceramic capacitor. https://en.wikipedia.org/wiki/Ceramic_capacitor. (Accessed 12 November 2019).
[46] X. Xu, J. Magee, A. Hoskins, M. Laps, A. Gurav, G.Y. Yang, C.A. Randall, Robust Class-I dielectric for high temperature applications, in: Proc. 29th Symp. Passive Compon. (CARTS USA), Jacksonville, FL, 2009.